Bin Zhu, Nathanael Leung, Winfried Kockelmann, Saurabh Kabra, Andrew J. London, Michael Gorley, Mark J. Whiting, Yiqiang Wang, Tan Sui

Understanding the residual stress distribution in laser welded Eurofer97 steel by neutron diffraction and Bragg edge imaging

Understanding the residual stress distribution in laser welded Eurofer97 steel by neutron diffraction and Bragg edge imaging

Bin Zhu, Nathanael Leung, Winfried Kockelmann, Saurabh Kabra, Andrew J. London, Michael Gorley, Mark J. Whiting, Yiqiang Wang, Tan Sui

Understanding the residual stress distribution in laser welded Eurofer97 steel by neutron diffraction and Bragg edge imaging

Bin Zhu[1], Nathanael Leung[1], Winfried Kockelmann[2], Saurabh Kabra[2], Andrew J. London[3],

Michael Gorley[3], Mark J. Whiting[1], Yiqiang Wang[3*], Tan Sui[1]*

[1] Department of Mechanical Engineering Sciences, University of Surrey, Guildford, Surrey, GU2 7XH, UK.

[2] Science and Technology Facilities Council (STFC) Rutherford Appleton Laboratory, ISIS Facility, Harwell, OX11 0QX, UK.

[3] United Kingdom Atomic Energy Authority, Culham Centre for Fusion Energy, Culham Science Centre, Abingdon, Oxon, OX14 3DB, UK.

* Corresponding author: t.sui@surrey.ac.uk; yiqiang.wang@ukaea.uk

Abstract

Eurofer97 steel is a primary structural material for the plasma facing-components of future fusion reactors. Laser welding is a promising technique that can overcome the challenges of remote handling and maintenance. However, the interaction of the induced residual stress distribution with the heterogeneous microstructure may degrade the mechanical performance of fusion components and this has not been fully revealed. Here, we characterised the residual stresses of as-welded and post-heat treated (PWHT) Eurofer97 joints using neutron diffraction and neutron Bragg edge imaging (NBEI) techniques. A typical M-shaped residual stress profile across the fusion zone, heat affected zone and base material is observed by neutron diffraction. A unique W-shaped residual stress distribution is captured by a high resolution NBEI technique within fusion and heat affected zones. The mechanistic connections between micro-hardness, microstructures and residual stresses has been established via correlative microscopy and nanoindentation measurements. The hardness value in the fusion zone of the as-welded sample was almost doubled (from 2.75 ± 0.09 GPa to 5.06 ± 0.29 GPa) by residual stress and fast cooling induced martensite. Conventional PWHT can release $90 \pm 3\%$ of residual stress but not fully restore the microstructures. This study paves the way to performing reliable structural integrity and failure prediction for critical structural components of future fusion reactors.

Graphical Abstract
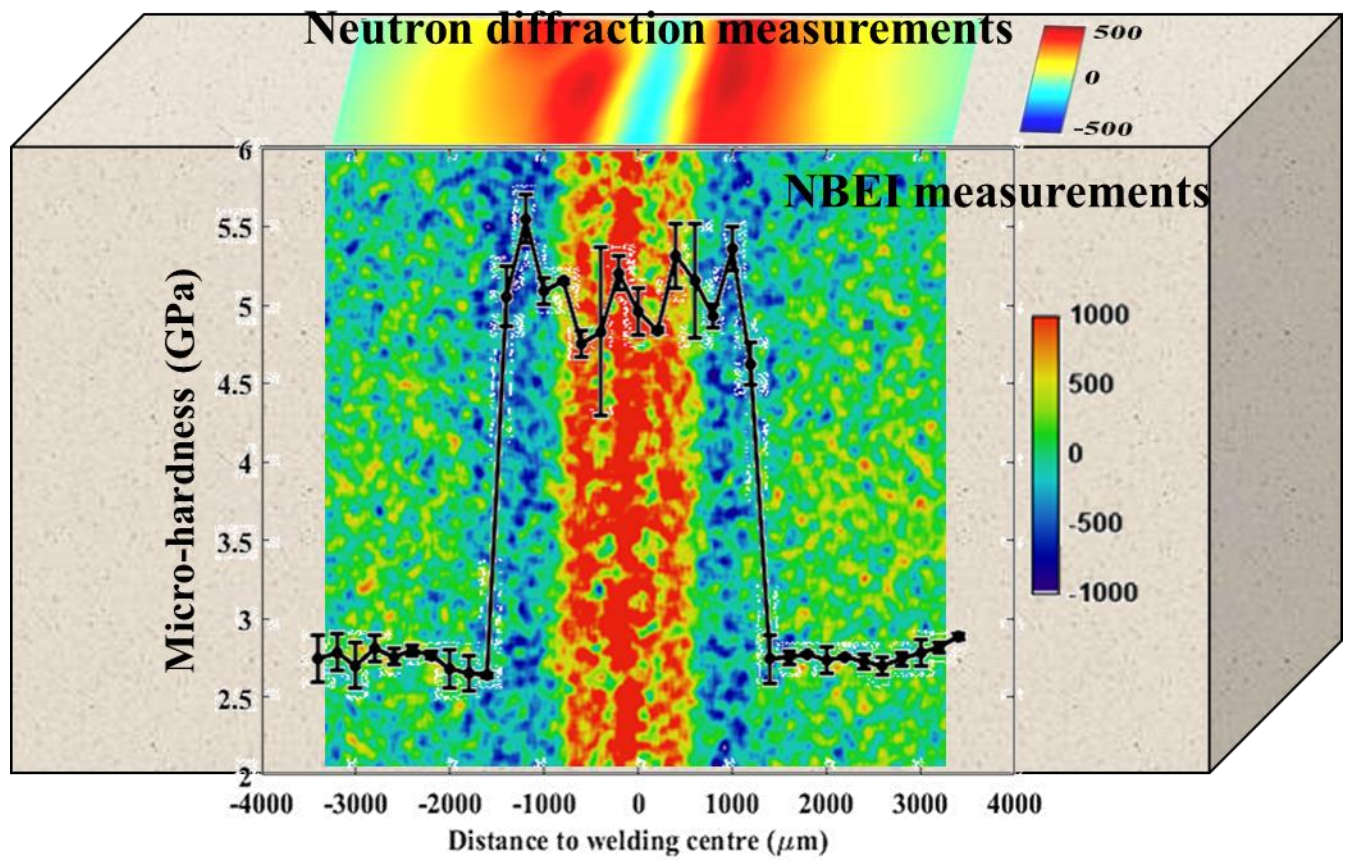
1   Introduction

Nuclear fusion is a potential substitute source of electricity production to solve dependence on fossil fuels and well-known environment issues resulting from carbon emissions. A range of key fusion tokamaks had been developed, from the Joint European Torus (JET), the International Thermonuclear Experimental Reactor (ITER) to the DEMOnstration power plant (DEMO). Reduced-activation ferritic/martensitic (RAFM) steels are modified to maintain the high Cr Grade 91 steel's heat resistance, irradiation resistance, favourable thermal physical, and high-temperature mechanical properties with inclusion of lower activation elements like W and Ta [1–4]. Eurofer97, one of the RAFM steels, is the European reference material for the in-vessel components (e.g. pipes, breeding blanket and divertor cassette) for the EU-DEMO [5–7]. The design of these in-vessel structures imposes intrinsic assembly difficulties, because of the internal grid structure and the meandering helium coolant circulation channels in the blanket plates [8]. The pipe connections of these breeding blanket components require quick, reliable welding and joining techniques to maintain structural integrity. Because of both the expected radiation levels and limited access, the joining and cutting process must be completed by remote in-bore tools for fabrication and maintenance [9].

Laser welding performed by a robotic device is one of the most promising techniques, which could perform both the welding and cutting operations. Compared with other welding techniques, laser welding gives rise to less distortion, enables full penetration single pass welds in thick sections, and has low heat input, leading to a narrow heat affected zone (HAZ). Previous studies have demonstrated the feasibility of remote laser tools for the manufacture and maintenance of the in-vessel components in fusion plants by laser welding [9–11]. This rapid welding process does, however, induce significant residual stresses up to c.800 MPa inside the welded steel [12]. The origin of this residual stress is predominantly the non-uniform deformation caused by thermal expansion and contraction, as well as a contribution from the martensitic phase transformation during the welding process [13]. The in-

4

service elevated temperatures aggravate creep relaxation cracking under the high tensile residual stress condition [14], whereas the compressive residual stress resists crack growth but leads to buckling [15]. Therefore, understanding the residual stress and its impact on the as-welded Eurofer97 is crucial to determining reliability and developing predictive tools for the in-vessel component of DEMO.

Neutron-based techniques have been used effectively to measure the residual strain in welds in a non-destructive way due to their high penetration and volume-averaged bulk information contents. The time-of-flight (TOF) method is especially valuable since multiple grain families are measured simultaneously [16]. Neutron diffraction can be used to determine the through-thickness residual stress by determining the residual strain in three dimensions throughout a sample [17]. The resolution measured by neutron diffraction is, however, limited by the gauge volume and the data acquisition time. Neutron Bragg edge imaging (NBEI) is a relatively new strain measurement technique, which follows similar principles to the TOF method, but has the capability to provide a two-dimensional (2D) strain map averaged over neutron path lengths via a pixelated detector in a single neutron beam exposure [18]. Due to a recent development of a micro-channel plate (MCP) neutron imaging detector [19], the NBEI technique provides residual stress maps in pixel resolution of 55 μm. Although a small number of studies have reported residual stress measurement of welds by the NBEI technique and compared the result with other techniques [20,21], combining the through-thickness residual stress in three dimensions and the high resolution local strain field to understand mechanistic connections between microstructure, residual stress, and micro-hardness has not been explored.

Considerable effort has been directed to the study of the integrity, mechanical properties, and microstructure of laser welded Eurofer97 [3,8,9,11,22,23]. For example, a good welding appearance with a few small gas-type defects were obtained after welding and a non-uniform hardness distribution were found across the joint [9]. The differences in phase, especially carbide, and microconstituent from the fusion zone (FZ) to the base material (BM) have been studied and the differences attributed to the non-uniform thermal gradient during the welding process [8]. Although these observations have

established the existence and effect of residual stress, the residual stress distribution in the as-welded Eurofer97 has not been explored in detail. Some attempt has been made to study the residual stress of {211} grain family at a depth of 1.25 mm below the surface on the laser welded Eurofer97 by neutron diffraction [12,24], but not the through-thickness residual stress distribution and high resolution residual stress map across the sample. More specifically, full insight into the relationship between micro-hardness, microstructure, and residual stress for laser welded Eurofer97 is lacking.

The motivation for this study is to quantitatively analyse the residual stress in laser-welded Eurofer97 steel using neutron-based techniques. Such techniques provide a deeper insight into the residual stress distribution in the material; with the NBEI technique offering a better description of the stress fields via the 2D map. In addition, the micro-hardness and microstructure are characterised to establish their intercedence. Post welding heat treatment (PWHT) was performed to release the residual stress, and the micro-hardness of this sample was measured. This information enables an understanding of how the PWHT alters the mechanical properties via the reduction of the residual stress. Finally, the understanding of the relationships between residual stress, microstructure, and mechanical properties will enable the manufacture of joints with improved service life.

2   Materials and methods

2.1   Materials

As-received Eurofer97 steel (made by Böhler Austria GmbH) with a composition Fe-0.11C-8.82Cr-1.08W-0.13Ta-0.48Mn-0.2V (in wt.%), was used in the present investigation. The detailed fabrication, rolling processes and heat treatment of as-received steel, has been described in a previous study [7]. The as-welded plate was butt welded perpendicular to the rolling direction by two as-received Eurofer97 steel plates, with dimensions $150 \times 75 \times 6$ mm^3. A 5 kW Yb-fibre laser source, with a welding speed of 1.2 m/min was employed for the single laser welding at TWI, which induces fully

narrow penetrated bead but less spatter and slight concave. As shown in Fig. 1a, two as-welded samples (#1 and #3) approximately ~$60 \times 40 \times 6$ mm^3 in size and two comb-shaped reference samples (#2 and #4) were cut from the as-welded plate by electrical discharge machining (EDM). In order to study the impact of residual stress on micro-hardness, the residual stress was relaxed by the PWHT. Samples #3 and #4 were annealed at 760 °C for 1.5 hours in vacuum followed by furnace cooling.

The samples which were used for microstructure and micro-hardness characterisation were cut from the samples #1 and #3 after neutron diffraction and NBEI experiments, following a suitable surface preparation, including mechanical polishing with a final vibration polishing step and etching with Vilella's reagent. Reflected light microscopy was used to distinguish the FZ, HAZ and BM regions of the as-welded sample. The microstructure of both the as-welded and PWHT samples were characterised by scanning electron microscopy, using a Jeol-7100 equipped with the electron backscatter diffraction (EBSD) detector (ThermoFisher) at the University of Surrey. The accelerating voltage for the EBSD test was 20 kV and the step size was approximately 0.6 µm. The denoising and filling non-indexing position were conducted by interpolating EBSD data using the MATLAB package MTEX 5.2.8 [25]. To account for the grain size, the grain boundary was re-constructed by smoothing the small grains less than five pixels and reducing orientation noise by a lower threshold of 15 °.

After the microstructural characterisation, micro-hardness tests were conducted using a nano indenter (Agilent G200) with a Berkovich indenter tip at the UKAEA's Materials Research Facility. Strain rate-controlled indentations were carried out to 2 µm depth using continuous stiffness mode (2 nm amplitude, 45 Hz frequency, 0.05/s strain rate) and made in an array (2×18) across the welds in steps of 200 µm. The micro-hardness values reported are an average of the depth resolved hardness from 1000 to 2000 nm deep. The error bars show the standard deviation of two indentation at same column of the array.
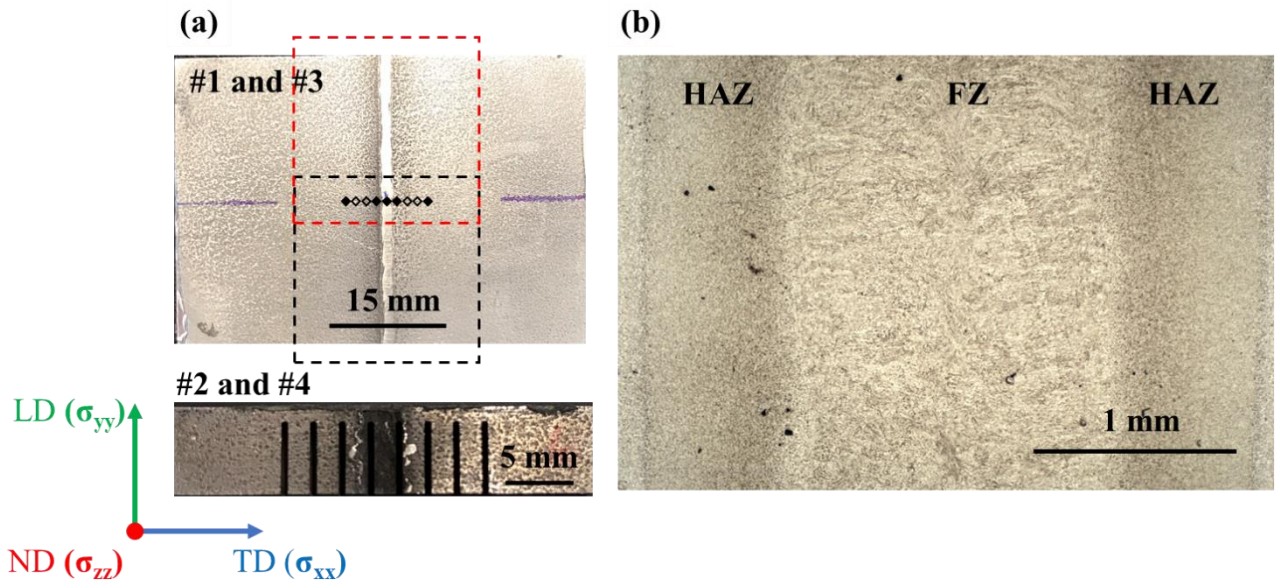
Figure 1 (a) Optical micrographs of an as-welded sample (top left) and a comb-shaped sample (bottom left). The black diamond-shaped spots (top left) indicate the position where the neutron diffraction data was acquired, and the red and black dash rectangles (top left) show the position of the residual strain maps using NBEI. (b) Optical microscopy image of distinct FZ and HAZ regions of the top view of as-welded sample.

2.2   Neutron diffraction

The residual lattice strain of both as-welded and PWHT samples along the longitudinal (LD), transverse (TD) and normal (ND) direction was measured by TOF neutron diffraction at the ENGINX beamline, Rutherford Appleton Laboratory, ISIS Neutron Source, UK. Fig. 1 shows the positions of the residual lattice strain measurements. There were nine data acquisition positions (unfilled and filled diamond spots) for the as-welded sample, and five (filled diamond spots) for the PWHT sample because the residual stress in BM region is considered uniformly distributed after PWHT. Fig. 2a shows the schematic of the experimental setup, where two detectors collect the diffracted neutrons at $\pm$ 90 ° relative to the incident beam. Two procedures were used to measure the lattice spacing in three dimensions. The sample was firstly mounted horizontally and oriented at 45° relative to the incident neutron beam. As shown in Fig. 2a, the through-thickness measurements were performed on the segment of the as-welded and the PWHT samples at distances of 1.72, 3.13 and 4.54 mm from the

surface on which the beam was incident. The neutron scattering gauge volume was $1 \times 1 \times 2$ mm^3, defined by an 1×1 mm^2 incident slit and 2 mm wide receiving radial collimators. To obtain sufficient neutron statistics for data analysis, neutron counts were acquired for 30 minutes at each data acquisition position in the HAZ and BM regions, and 45 minutes was chosen for collection at the data points in the FZ region. The axial detector recorded the strain along TD, while the radial detector recorded the strain along ND. In order to calculate the residual stress in three dimensions, the sample was rotated 90º around the ND axis to measure the strain along the LD acquired by the axial bank and the acquisition time remained the same for each region. The residual stress measurements in three directions were performed on the same segment and position for both as-welded and PWHT samples by the same setup. The comb-shaped reference samples, in which the macroscopic residual stress was assumed to be totally relieved, was also measured to determine the reference lattice parameter d_0. Data was analysed by Rietveld refinements via routines written in Open Genie [26–28]. As show in Fig. 2b, the multi-peak fitting was obtained by adopting the Powley-type analysis of five peaks and the lattice spacing of each grain family was obtained using single-peak fitting (a Voigt peak shape combined with an exponential function) [29,30]. To study the macro- residual stress, the lattice spacing of {110} and {211} grain families were selected for calculating the residual stress. The residual strain ε^{hlk} (in microstrain) was determined by:

$$\varepsilon^{hlk} = \frac{d^{hlk} - d_0^{hlk}}{d_0^{hlk}} \times 10^6 \qquad \qquad \text{Eq. 1}$$

where d^{hlk} is the lattice spacing and d_0 is the reference lattice spacing.

The stiffness tensor that is formed by diffraction elastic constants and presented in Voigt matrix notation shows the relationship between lattice strain and stress [31]. There are three independent fourth-order elastic constants for BCC structures and the values of the three for Eurofer97 are C_{11} = 285.2 GPa, C_{12} = 125.9 GPa and C_{44} = 120.3 GPa [4]. The stiffness tensors in the crystal reference frame ({110} and {211}) are derived from the stiffness tensor in the specimen reference frame by

transforming the matrix according to Bunge angles [31]. The Bunge angles for {110}[110] and {211}[211] diffraction planes were calculated by MATLAB and the stiffness tensors in crystal reference frame was calculated by:

$$[C_{hlk}] = [C][R_{hlk}] \hspace{3cm} \text{Eq. 2}$$

where C is the stiffness tensor in the specimen reference system, C_{hlk} is the stiffness tensor in crystal reference frame and R_{hlk} is the transformation matrix according to Bunge angles of diffraction planes. The lattice stress for specific diffraction planes was then determined by Hooke's law:

$$[\sigma_{hlk}] = [C_{hlk}][\varepsilon_{hlk}] \hspace{3cm} \text{Eq. 3}$$

2.3   Neutron Bragg edge imaging (NBEI)

The NBEI experiment was conducted at the IMAT beamline at Rutherford Appleton Laboratory, ISIS, UK [20]. A microchannel plate (MCP) detector with the field view of is 28×28 mm^2 and pixel resolution of 55 µm (512×512 pixels) was used as the main TOF imaging camera [19]. The strain map with spatial resolution of ~ 200 µm was measured by the TOF method with an *L/D* value of 166, where *L* is the distance from the pinhole collimator to sample and *D* is aperture diameter [32]. A high-purity ferritic iron rod of 10 mm diameter was measured first to calibrate the length of the flight path [20]. Two maps were then collected on each sample, as-welded and PWHT, with ~5 mm overlap, illustrated by red and black rectangles (see Fig. 2c). An open-beam data set was acquired, with the sample removed. A stack of 2881 radiographs was collected for each run, requiring four hours for adequate neutron counting statistics. The image stacks of the sample data and the open-beam data stacks were processed using ImageJ [33], to obtain transmission maps by dividing the sample stack by the open beam stack. As shown in Fig. 2d, a Bragg edge spectrum is then plotted as transmission as function of wavelength, for a single pixel, combined 'macro-pixel' composed of several pixels, or a

larger region of interest. The position of a Bragg edge was determined by fitting the Bragg edge spectrum via an analytical function [34]:

$$T(\lambda) = C_1 + C_2 \left[erfc(\frac{\lambda_0 - \lambda}{\sqrt{2}\sigma}) - \exp\left(\frac{\lambda_0 - \lambda}{\tau} + \frac{\sigma^2}{2\tau^2}\right) \times erfc(\frac{\lambda_0 - \lambda}{\sqrt{2}\sigma} + \frac{\sigma}{\sqrt{2}\tau}) \right] \qquad \text{Eq. 4}$$

where λ is lambda edge position, σ is the Bragg edge width, τ is the edge asymmetry, C_1 is edge height and C_2 is edge pedestal (see inset Fig 2d). The residual strain was determined pixel-by-pixel according to the Bragg edge position by the Eq 5, and the map was generated by a C++ fitting tool, TPX_edgefit, by using a macro-pixel size of 5 pixels and a running average with steps of 55 um [34]. The reference Bragg edge position was extracted from a far-field welding affected region in the BM zone.

$$\varepsilon^{hlk} = \frac{\lambda^{hlk} - \lambda_0^{hlk}}{\lambda_0^{hlk}} \times 10^6 \qquad \text{Eq. 5}$$

where λ is the Bragg edge position of the sample, λ_0 is the reference Bragg edge position. It is worth noting that the NBEI yields the strain component in beam direction only (i.e. ND).
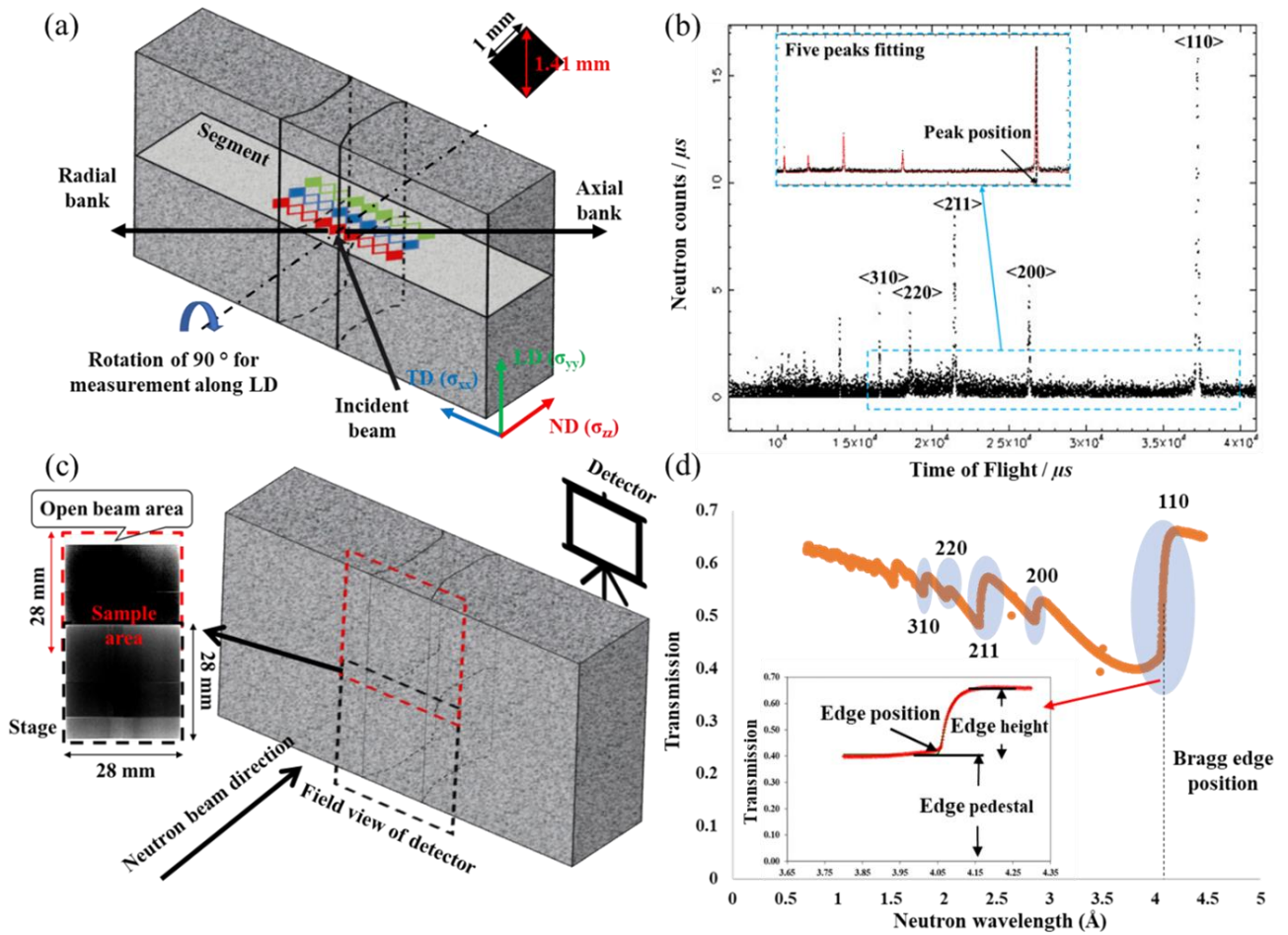
Figure 2 (a) A schematic of the neutron diffraction experiment setup and data acquisition position. Three through-thickness line-scans at the different distances to beam incident surface were performed. The data was acquired at both filled- and unfilled-spots position for the as-welded sample, while only at filled-spot positions for the PWHT sample. The diffraction data was recorded by two detector banks, labelled 'axial' and 'radial', yielding the strains along TD and ND. In order to measure residual stress along LD, the sample was rotated 90 ° around ND and three line-scans were performed at the same data acquisition position. (b) Lattice parameter and lattice spacings were extracted by multiple peak fitting. (c) Neutron Bragg edge imaging (NBEI) experiment setup. The red and black dashed rectangles illustrate the two mapped areas cover the welding affected region. The two images on the left are the transmission data recorded and saved by the detector. (d) An example of Bragg edge fitting for the {110} grain family. The Bragg edge position is obtained as one of five fitting parameters: edge position, edge height, edge width, edge pedestal and edge asymmetry (equipment parameter).

3 Results

3.1 Microstructure and hardness characterisation

Figures 3 and 4 show the microstructure and hardness distribution across the welds of as-welded and PWHT samples, respectively. As illustrated in Fig. 3a and Fig. 3b, irregularly columnar

12

bainite/martensitic packets/laths, which grew during rapid cooling, were formed in the FZ region, whereas equiaxed tempered martensitic/ferritic grains were present in the HAZ and BM regions. Because of partial austenisation and tempering occurred in the HAZ region, the quenched and tempered martensite were observed together. In the BM region, grain boundaries and martensitic laths were decorated by a large number density of precipitates, which demonstrated the similar crystallographic microstructures with as-received Eurofer97. The grain size of the FZ, HAZ and BM regions was determined by the inverse pole figure (IPF) maps in Fig. 3b using the mean linear intercept method [35]. The average grain size was found to significantly decrease from ~15 ± 3 μm at the FZ region to ~6 ± 1 μm at the HAZ region but increased at the BM region to ~7 ± 1 μm. Fig. 3c displays the pole figures (PF) of the (110) and (211) crystal plane normal of the FZ and HAZ regions. It is evident that the (110) crystal plane exhibits a stronger texture at the FZ region, which reaches around 4 multiples of a random distribution (MRD), but the intensity in the HAZ region decreases to around 1.8 MRD. Additionally, the highest intensity of (110) plane normals in both FZ and HAZ regions occurs along the direction which is parallel to the ND in the specimen reference frame. In contrast, the highest pole densities of (211) in both FZ and HAZ regions are lower than that of the (110) crystal plane, which are around 2.2 and 1.2 MRD respectively.
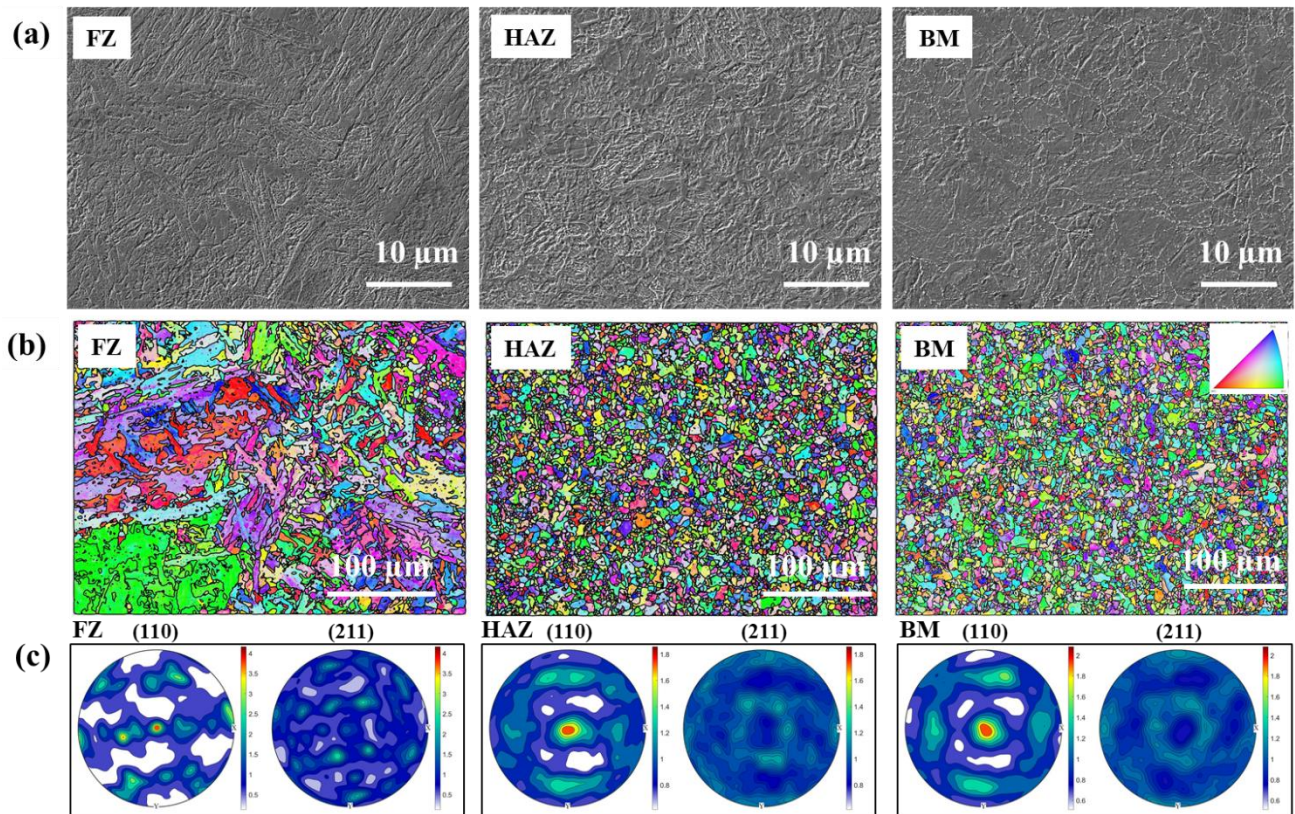
Figure 3 Microstructure of as-welded sample. (a) Microstructure at FZ, HAZ and BM regions acquired by SEM. (b) IPF maps at the FZ, HAZ and BM regions. (c) Corresponding PF at the FZ, HAZ and BM regions.

The micro-hardness of both the as-welded and PWHT samples are summarised in Fig. 4. The micro-hardness profile of the as-welded sample increases from 2.75 ± 0.09 GPa in the BM region to 5.06 ± 0.29 GPa in FZ and HAZ regions. The hardness at the FZ and HAZ regions is reduced significantly by the selected PWHT to 3.25 ± 0.11 GPa. A significant jump is found at the interface between the HAZ and BM on the as-welded sample, while a gradual drop occurs at the same position for the PWHT sample. To reveal the effect of residual stress and microstructure on micro-hardness, Fig. 4b illustrates the micro-hardness differences at the FZ region by the load-displacement curves of as-welded and PWHT samples. This difference is attributed to the microstructure and residual stress hardening. Comparing with the curve at the BM region, the total hardening and hardening caused by PWHT microstructure is obtained. Fig. 4c and Fig. 4d shows the grain structures of the PWHT sample in the FZ and HAZ regions, respectively. In comparison, for the as-welded sample the grain size remains the same after PWHT. The PFs in Fig. 4e and Fig. 4f shows that the {110} planes are still textured in the

14

FZ region, with pole density maxima ~ 3 MRD, while moving to the HAZ region, the intensity of texture decreases to the 1.5 MRD. By contrast, the texture of {211} planes is significant lower in the FZ and HAZ regions where the highest intensity is ~ 2 and ~ 1.2, respectively. As such, the pole density distribution is similar to the as-welded sample.
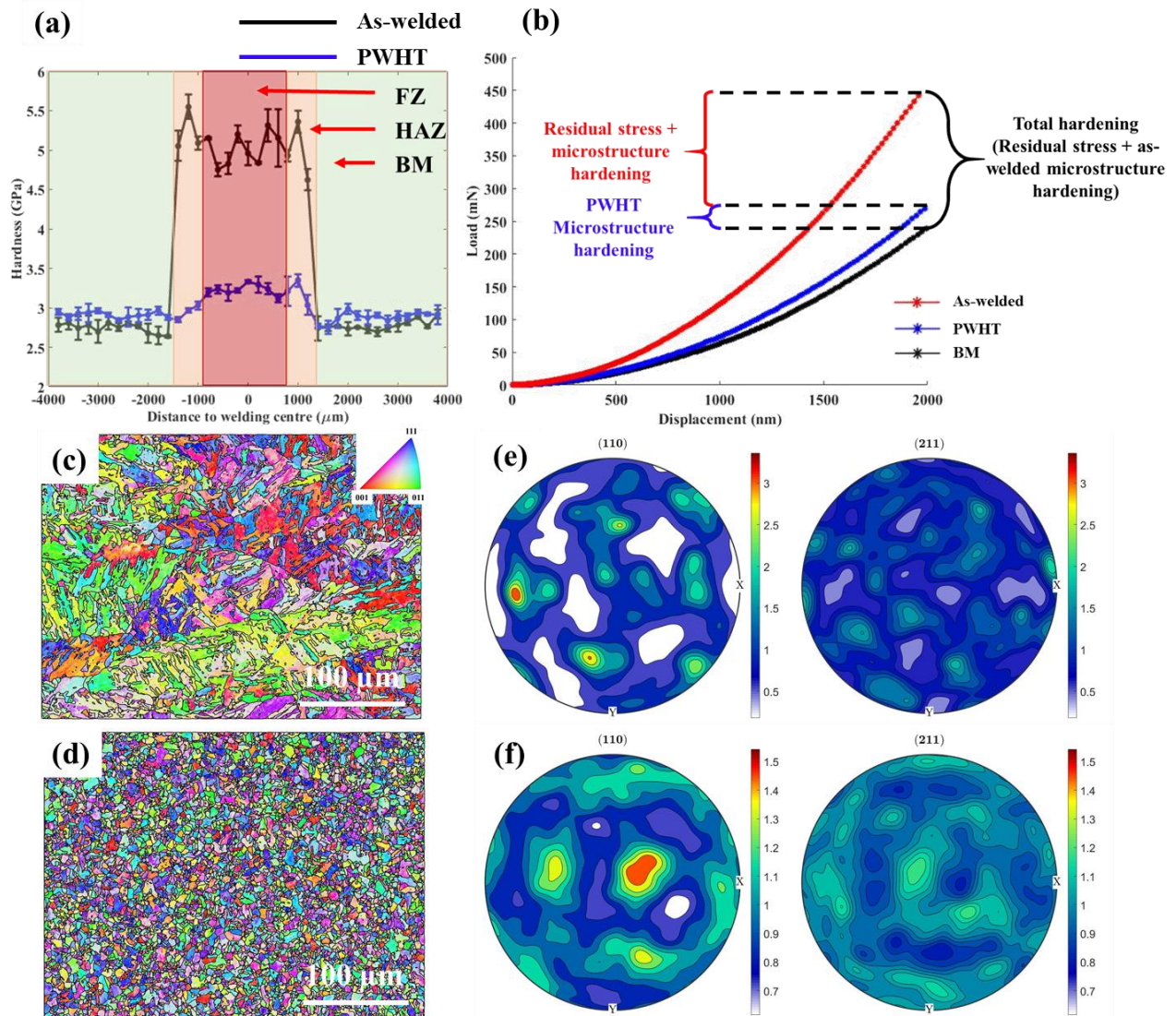

Figure 4 (a) Micro-hardness distribution of as-welded and PWHT samples. (b) load-displacement curves derived from the BM and FZ of as-welded and PWHT samples, respectively. (c) and (d) IPF maps of PWHT sample at FZ and HAZ regions. (e) and (f) PF derived from relative EBSD maps at FZ and HAZ regions, respectively.

3.2   Residual stress distribution revealed by neutron diffraction

The lattice spacings derived from multi-peak and single-peak fitting approaches corresponding to crystallographic planes {211} and {110} were used to calculate the residual stress. The through-thickness residual stress profiles in three dimensions of the as-welded and PWHT samples are shown in Fig. 5a and Fig. 6a, respectively. The σ_{xx}, σ_{yy} and σ_{zz} represent the residual stress along TD, LD and ND, respectively, and the red, blue and green symbols and lines represent the residual stress at different distances from the beam incident surface. The residual stress profiles derived from single-peak fitting shown in Fig. $5a_1$ and Fig. $5a_2$ show similar M-shaped symmetry, whereas the profiles of multi-peak fitting (Fig. $5a_3$) are less distinct. Additionally, the residual stress magnitude solely fitted by {211} planes is larger than that fitted by {110} diffraction planes and multi-peaks fitting. The highest residual stress derived from {211} diffraction planes is σ_{yy}, 580 ± 20 MPa, whereas the lowest residual stress is found to be both σ_{xx} and σ_{zz} residual stress components, which is 595 ± 20 MPa. The uncertainty is from the determination of peak position.

Residual stress maps of σ_{xx}, σ_{yy} and σ_{zz} components on the segment plane of the as-welded and PWHT sample were plotted with the values from neutron diffraction measurements by MATLAB in Fig. 5b and Fig. 6b respectively, using the three through-thickness line-scan measurements. As illustrated in Fig. 5b, the residual stress extracted from the single-peak follows a similar distribution at different distances from the beam incident surface, and the σ_{yy} is obviously higher than in other directions, and compressive residual stress is found within the FZ region. Moving away from the centre, the residual stress gradually transforms and reaches tension and eventually decreases to zero in the BM region. The residual stress extracted from multi-peak fitting exhibits the less obvious trends.
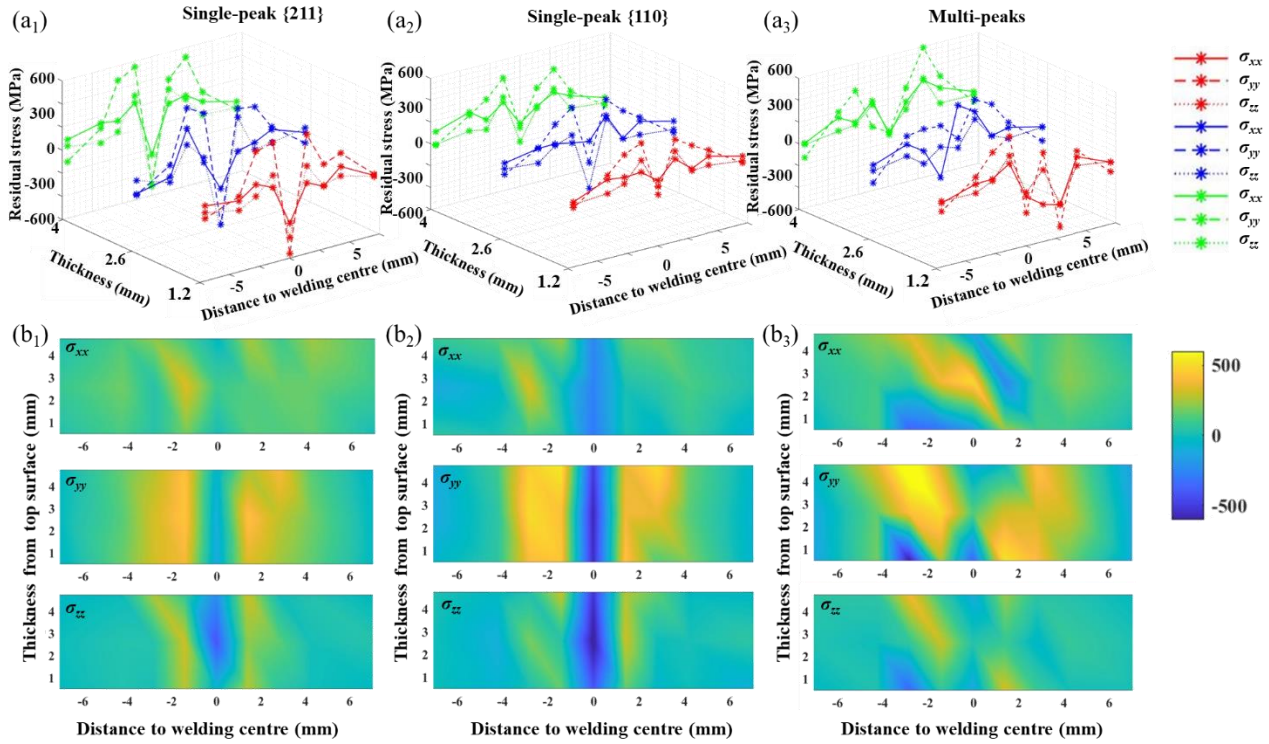
Figure 5 Residual stress of σ_{xx}, σ_{yy} and σ_{zz} components of as-welded sample derived from neutron diffraction by single-peak and multi-peak fitting approaches. (a) The through-thickness residual stress distribution extracted at three different distances to beam incident surface. (b) The residual stress on the segment plane.

Figure 6a indicates that the residual stress has been relaxed significantly after PWHT. Although the values are very low, the residual stress still exists around the welding centre, ranging from -50 MPa to 100 MPa as measured by both single-peak and multi-peak analyses. In general, the profile of the residual stress in three dimensions are of a similar magnitude and follow the same overall trend. The variation of the three through-thickness profiles in Fig. 6a$_3$ is, however, higher than that in Fig. 6a$_1$ and Fig. 6a$_2$. For the {211} planes (Fig. 6a$_1$), the blue residual lattice stress profile is different in shape, compared with the red and the green curves, while they are similar for the {110} planes (Fig. 6a$_2$). Fig. 6b shows the residual stress maps of the measured segment plane, which illustrates that the residual stress has been relieved.
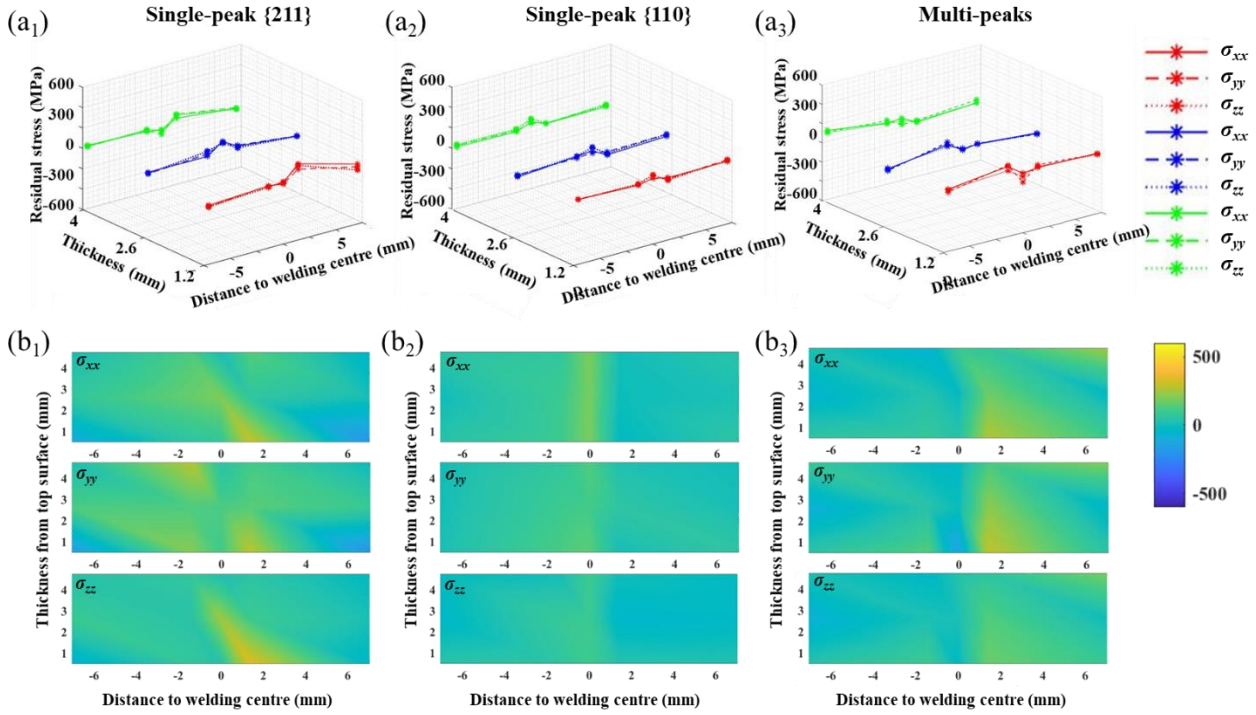
Figure 6 Residual stress distribution of σ_{xx}, σ_{yy} and σ_{zz} components of the PWHT sample derived from neutron diffraction by single-peak and multi-peak analyses. (a) The through-thickness residual stress distribution extracted at three different distances to beam incident surface. (b) The residual stress on the segment plane.

3.3 Residual stress distribution revealed by neutron Bragg edge imaging (NBEI)

The NBEI residual strain maps derived from {211} and {110} diffraction planes along ND of as-welded sample are shown in Fig. 7a. In both Fig. 7a$_1$ and Fig. 7a$_2$, the distinct tensile residual distributes around the centre line of the weld, in tension within about 1.5 mm length, and balanced by compressive stress further away. The residual strain is more or less uniformly distributed along LD. The pixel resolution of the map is around 55 µm and the spatial resolution of the NBEI technique is about 200 µm due to the large macro-pixel size used in combination with a running average. To reveal the distribution across the weld clearly, the 2D lattice spacing and residual strain maps are converted to 1D profiles by averaging values over LD and plotted in Fig. 7b and Fig. 7c respectively, namely NBEI high-resolution. The NBEI high-resolution 1D profiles are in the same pixel resolution (55 µm) as the map. To compare with the result from neutron diffraction, the NBEI high-resolution 1D profiles

18

are converted to the NBEI moderate-resolution profiles (green curves in Fig. 7b and Fig. 7c) by reducing the pixel resolution to 1.4 mm which is in the order of the gauge volume length of neutron diffraction. The lattice spacing (red in Fig. 7b) extracted from neutron diffraction are also added in the figure. Fig. 7b shows the comparison of lattice spacing, where the trend of the NBEI is consistent with that of neutron diffraction, while the absolute lattice spacings are slightly but systematically lower for NBEI. Fig. 7c shows comparison of residual strain where the residual strain profile from neutron diffraction data was re-calculated by employing far-field welding affected region as a reference with a red dashed line. It is noticeable that the NBEI high-resolution profiles show a W-shaped variation around the welding centre, which is lacking in the neutron diffraction measurement. Furthermore, the residual strain derived from the {110} diffraction plane is higher (1500 $\mu\varepsilon$) at the very centre of welding line compared to other areas.

The residual lattice strain maps and profiles for the {211} and {110} planes of the PWHT sample are plotted in Fig. 8 in the same manner. It is clear that residual strain reduces significantly after PWHT. The maps derived from the {110} planes show, however, a tensile residual strain up to 600 $\mu\varepsilon$ at the very centre of welding line.
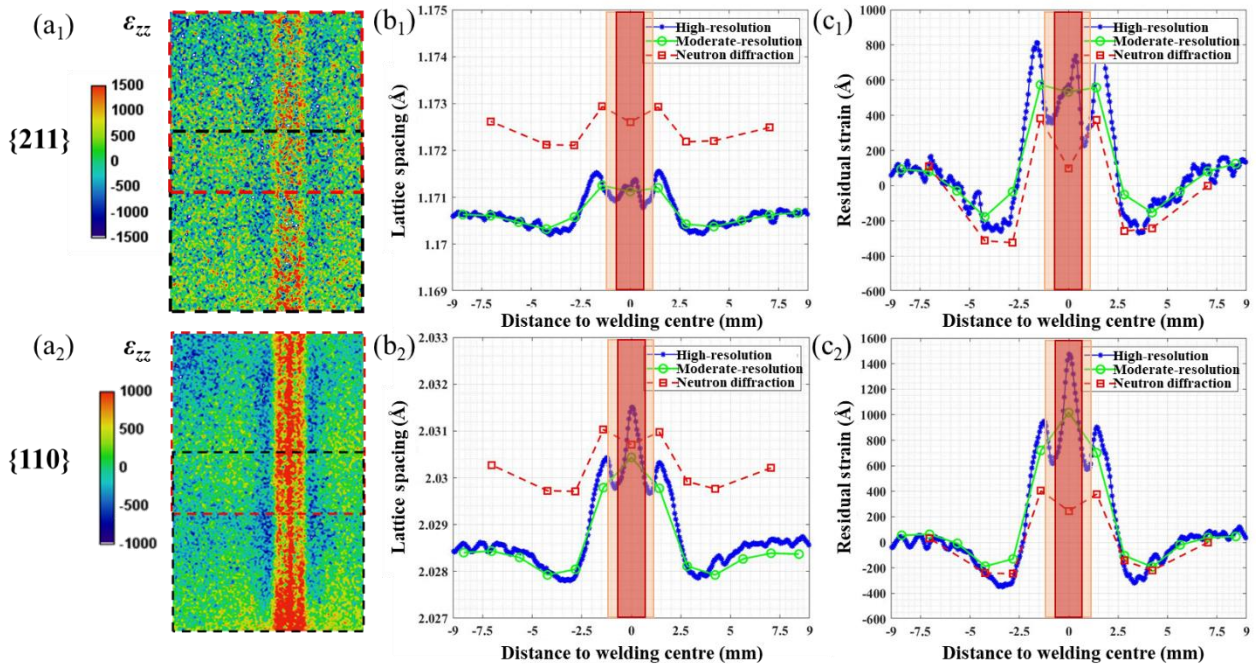
Figure 7 Residual strain maps and strain profiles of the as-welded sample measured by NBEI. (a_1) and (a_2) Strain maps along ND calculated from lattice spacings of {211} and {110} grain families. (b_1) and (b_2) Lattice spacing distribution across the welded region by averaging over LD. The NBEI high-resolution profile is plotted in blue and the NBEI moderate-resolution profiles is plotted in green. The lattice spacing distribution from neutron diffraction is plotted in red for comparison. (c_1) and (c_2) Residual strain distribution measured by NBEI is plotted in blue and green by the same method as in (b) and the residual lattice strain measured by neutron diffraction is re-calculated and plotted in red.
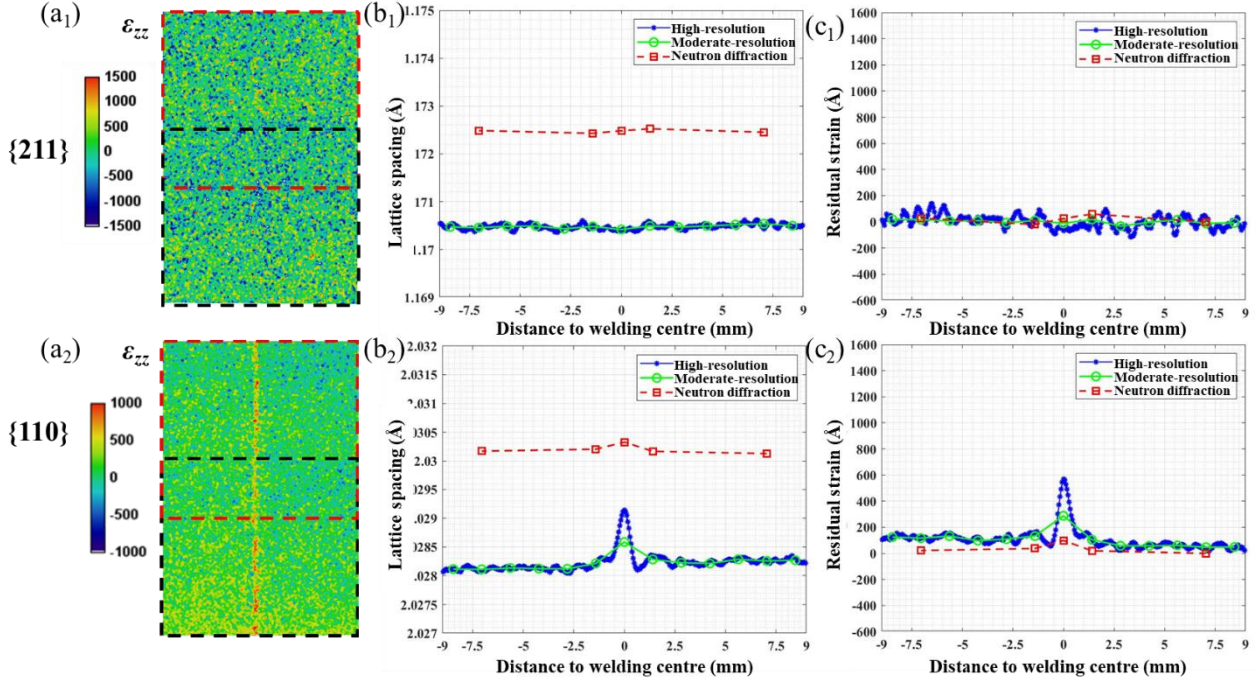
Figure 8 Residual strain maps and strain profiles of the PWHT sample measured by NBEI. (a_1) and (a_2) Strain maps along ND. (b_1) and (b_2) Lattice spacing distribution converted by 2D strain map and measured by neutron diffraction. (c_1) and (c_2) Residual strain distribution from NBEI and neutron diffraction. The residual lattice strain and lattice spacing distribution profiles are plotted in the same way as in Fig. 7.

4   Discussion

4.1   Residual lattice stress and strain distributions across FZ, HAZ and BM regions

All the profiles in Fig. 5a and Fig. 7a show that the residual stress caused by the single laser welding acts over approximately 2.5 mm from the welding centre, and manifests itself as M-shaped curves; strongly in compression at the FZ region (~ 600 MPa) and changing to tension and reaching maximum at the BM region (~ -600 MPa) just outside the HAZ. The shrinkage, quenching-induced martensitic and bainitic phase transformations and γ-α phase transformation during the cooling process affects both the magnitude and trend of the residual stress profiles [36,37]. Transformation-induced residual stress, which usually leads to the expansion of the carbon steel, is dominant in compression, whereas shrinkage-induced residual stress is usually in tension. As a result of high heat input and the rapid

cooling process of laser welding, the shrinkage and phase transformation effectively occur simultaneously contributing to the M-shaped residual stress profile.

The single pass laser welding induces the narrow FZ and HAZ, which is approximately 5 mm. In comparison the hybrid laser welded Eurofer97 steel, with a power of 4 kW, had a FZ and HAZ of width ~12 mm [12]. The single pass laser welding produces a narrower FZ and HAZ region than the hybrid-laser welding, whereas the magnitude of the residual stress remains for the same as the sample welded by hybrid laser welding (600 MPa). A similar phenomenon is also found on the single laser and hybrid laser welded P91 steel with 7 kW heat input, where narrow FZ and HAZ are generated by single pass laser welding and the residual stress induced by the two techniques are similar [38].

The residual stress distribution in Fig. 5a also illustrates a similar magnitude and trend at different thicknesses. This indicates full penetration of the sample during welding generates similar widths of FZ and HAZ regions. Similar results are also found in ferritic steel welded by high heat-input joining techniques [17]. Comparison of the residual lattice stresses in the three directions, TD, LD and ND, (Fig. 5b), reveals that the transversal and normal residual stress profiles are similarly M-shaped like the longitudinal profile, but exhibiting lower tensile residual stress levels as expected. This is attributed to the unbalanced compressive plastic flow that occurs in front of the weld pool during the welding thermal cycle leading to a higher tensile residual stress at the interface of the HAZ and BM which is in agreement with laser-welded P91 steel [13].

Differences in magnitude and distribution of the residual stress profile are found in Fig. 5a, derived by single-peak fitting of {211} and {110} as well as by multi-peak analysis. Micro-residual stress can result, for example, from plastic deformation of a material, leading to peak shifts, whilst the residual stress measured by neutron diffraction is the sum of the macro- and micro- scales [39]. Different grain families have different sensitivities to intergranular stresses. The multi-peak fitting is derived from five grain families and some of these are seriously affected by the micro strain, whereas the {211} and {110} grain families are recommended to represent the residual stress on the macroscale. The residual

22

stress profile derived from {211} and {110} grain families exhibit the same trend, but the magnitudes differ to a small extent. On the other hand, similar difference of two grain families are also observed in the NBEI strain profiles (blue curve in Fig. 7b$_1$ and Fig. 7b$_2$) where the profile of {211} is lower than that of {110}. Moreover, the residual strain profile of the {110} grain family acquired by NBEI at the welding central position of the FZ region is higher than at any other point, but this is not observed for {211} planes. Such a phenomenon is attributed to the texture, which is more pronounced in the FZ region and weaker further away, as illustrated in Fig. 3c. Although texture is not directly related to the measurement of strain, it can affect the Bragg edge position, which is defined exclusively by the planes oriented perpendicular to the incident beam [40]. The peak fitting for neutron diffraction is, however, less affected in the FZ region, which does highlight that Bragg edge fitting for NBEI is much more sensitive to texture than Bragg peak fitting for neutron diffraction.

PWHT is usually applied to modify the as-weld microstructure and relax residual welding stresses in order to impart reliable properties. Fig. 4c indicates that the grain size remains the same after PWHT. The residual strain profile from the {110} grain family (Fig. 8c$_2$) is obviously higher at the FZ central position than elsewhere, which shows the same trend as that in Fig. 7c$_2$. This is also attributed to the texture distribution in the welds after PWHT, which follows the same argument as made for the as-welded sample above. Fig. 4e and Fig. 4f show similar pole densities in the FZ and HAZ regions of the PWHT sample. Although the grain size and texture were not changed significantly, the selective PWHT was effective at releasing the residual stress. The measurements by both neutron-based techniques demonstrate that the high residual stress disappeared in the PWHT sample, as expected, showing that PWHT is very effective in relaxing residual stresses, as shown in Fig. 6 and Fig. 8.

4.2   Comparison between neutron diffraction and neutron Bragg edge imaging

Both techniques measure the strain using a TOF method, providing information from the interior but with different spatial resolution and gauge volume. Neutron diffraction selects a gauge volume length of 1.41 mm along the beam direction by controlling the incident slits and by using a radial

23

collimator (see inset Fig. 2a), whereas for NBEI the strain is averaged over the whole chord through the sample. The spatial resolution of ~200 µm for NBEI is controlled by the value of *L/D* and the choice of the macro-pixel binning of the 55 µm pixels of the MCP detector. Comparing the profile from neutron diffraction (Fig. 5) with the NBEI high-resolution profiles in Fig. 7, illustrates the benefit of ~10 times higher resolution for NBEI, as it allows observing the W-shaped variation of residual lattice strain at the sub-region (within 0.5 mm), i.e. melted, fully austenitised, partially austenitised, and tempered regions, of the FZ and HAZ regions.

It is also noted from Fig. 5 and Fig. 7, the residual lattice strain/stress results reveal significant differences between the two techniques. This can be attributed to the different reference lattice spacing data employed, where the location-dependent d_0 from the comb-shaped sample was used for the neutron diffraction whereas for NBEI a d-value from the BM region was employed. There are four ways widely recommended for obtaining reference lattice spacings. These are measurement at a far-field welding affected region, measurement on a stress-free powder or filings, measurement on a thin cube, or use of the teeth of a comb with the application of stress balance [41]. Given that diffraction-based residual strain/stress measurements account for not only elastic strain, but also inelastic strain like phase transformation, obtaining a reference lattice spacing is a critical part of the procedure [42,43]. Additionally, as a result of the difference in thermal history during the welding, the inelastic strain varies with the position. With a location-dependent d_0 spacing, the effect of inelastic strain and microstructure can be corrected in the residual strain/stress calculation. Since the high-resolution of the NBEI residual strain map is, however, derived by pixelated image-based calculation, location-dependent d_0 spacing tended to be poorly correlated during the calculation. Therefore, the reference lattice spacing was determined by local far-field region for the NBEI.

To compare the results from the two techniques directly, the lattice spacing profiles and residual strain profiles of neutron diffraction are re-processed and presented in Fig. 7 and Fig. 8 by employing the same resolution and penetration as for NBEI, as well as the reference lattice spacing from BM. The

trend of re-calculated results of the as-welded sample (red curve in Fig. 7c) is in good agreement with that of hybrid-laser welded Eurofer97 sample measured by neutron diffraction without located-dependent reference lattice spacing [12,24,44]. It is also found that the lattice spacing and residual lattice strain profile averaged over the sample thickness of both as-welded and PWHT samples from neutron diffraction are in a good agreement with the NBEI moderate-resolution profiles. The discrepancy between the two neutron-based techniques is within 0.14%, which is acceptable.

4.3   Correlation of microstructure, micro hardness and residual stress

Micro-hardness is quite sensitive to the microstructural changes taking place throughout the welds. Fig. 4 shows that the micro-hardness distributions of both samples, from which the FZ and HAZ regions are significantly higher than that at BM region. This is attributed to both microstructural variation and spatial variation in residual stress [45,46]. The laser welding provides high heat input leading to a range of metallurgical transformations occurring in the FZ and HAZ, which are expected to have inhomogeneous microstructural distributions after the welding process [24]. The bainitic constituent which is assumed to contain dislocation-rich ferrite and cementite is largely confined to the FZ, whereas the quenched and tempered martensite dominate the HAZ (Fig. 3a). Moreover, the grain size at the FZ is larger than that at HAZ by approximately three-fold, which in principle means a lower hardness according to Hall-Petch relation [47,48]. The micro-hardness at the FZ and HAZ regions, however, remains the same. This is attributed, at least in part, to the hardening by compressive residual stress in the FZ region and softening by tensile residual stress in the HAZ region. Moving to the BM region, since temperature here is lower than the lower critical temperature (A_{c1}) and the tensile residual stress reaches maximum, a steep drop in micro-hardness occurs. A similar phenomenon also happened on laser welded P91 steel [13]. On the other hand, the micro-hardness at the weld was reduced significantly by the PWHT but remain same at the BM region. This is attributed to both residual stress relief and microstructure changes. The results (Fig. 6 and Fig. 8) demonstrate that the

residual stress is fully relieved after PWHT and high temperature PWHT results in the formation of equiaxed ferritic grains from lath-shaped martensitic grains and coarsening of precipitates [49].

A comparison of load-displacement curves (Fig. 4b) reveals the contributions of the residual stress and microstructure to the hardening phenomenon at the FZ region. The laser welded material is harder because of both residual stress and of the as-welded microstructure, whereas PWHT only hardens material by distinct features of the microstructure. The micro-hardness reduction between as-welded and PWHT samples has two aspects, including residual stress relief and changes from as-welded microstructures to PWHT microstructures. A full model that can account for the relative contributions of residual stress and microstructure is the subject of ongoing research.

5   Conclusions

The through-thickness residual stress and high-resolution local strain field of as-welded and PWHT Eurofer97 samples were studied using two neutron-based techniques. The micro-hardness and microstructure were characterised, in order to understand the residual stress distribution and its impact on micro-hardness. The key results are summarised as follows.

1. Using neutron diffraction, the through-thickness residual stress distributions in three directions were obtained in the as-welded and PWHT Eurofer97 samples. The as-welded sample shows a M-shaped residual stress profile and its magnitude in the longitudinal direction is the most significant: 595 ± 20 MPa of compressive stress at along centre line of the FZ region and 580 ± 20 MPa of tensile stress at the interface of HAZ and BM regions.

2. Using the NBEI technique, the 2D residual strain map has been generated for the as-welded and PWHT Eurofer97 samples. The strain maps show distinct differences in the FZ, HAZ and BM regions. 1D profiles, extracted from a 2D map, show a W-shaped variation in the FZ and HAZ regions, which is not seen in the neutron diffraction data.

26

3. The lattice spacing results derived from the NBEI technique reveals good agreement with the data from neutron diffraction. The discrepancy between the two neutron-based techniques is within 0.14%, which is acceptable. Although there are principal limitations because of texture in these materials, better results can be achieved in future with neutron sources of higher brilliance, by improvements in transmission detector technology, and further development of Bragg edge data analysis tools.

4. The understanding of the mechanistic connections between micro-hardness, microstructure and residual stress has been broadly established. The as-welded sample in the FZ region is hardened by residual stress and microstructural features. Selective PWHT is capable of relieving the residual stress, but the microstructures are not restored thoroughly. The material in the FZ and HAZ regions is still hardened by lath-shaped martensitic phase and grain size after PWHT.

Acknowledgements

Author Contributions

Tan Sui (TS), Yiqiang Wang (YW), Mike Gorley and Mark Whiting conceived the study. Bin Zhu (BZ) and YW prepared the samples. Saurabh Kabra, YW and BZ carried out the experiment on ENGIN-X and Nathanael Leung, Winfield Kockelmann, YW and BZ performed the experiment on IMAT. BZ and Andrew London performed nanoindentation at UKAEA's Materials Research Facility. BZ performed the data analysis and wrote the manuscript with TS and YW. All authors edited and commented on the manuscript. The authors declare that they have no competing interests.

Reference

[1]   P. Fernández, A.. Lancha, J. Lapeña, M. Serrano, M. Hernández-Mayoral, Metallurgical properties of reduced activation martensitic steel Eurofer'97 in the as-received condition and after thermal ageing, J. Nucl. Mater. 307–311 (2002) 495–499. https://doi.org/10.1016/S0022-3115(02)01013-9.

[2]   A. Zeman, L. Debarberis, J. Kočík, V. Slugeň, E. Keilová, Microstructural analysis of candidate steels pre-selected for new advanced reactor systems, J. Nucl. Mater. 362 (2007) 259–267. https://doi.org/10.1016/J.JNUCMAT.2007.01.068.

[3]   S. Wu, J. Zhang, J. Yang, J. Lu, H. Liao, X. Wang, Investigation on microstructure and properties of narrow-gap laser welding on reduced activation ferritic/martensitic steel CLF-1 with a thickness of 35 mm, J. Nucl. Mater. 503 (2018) 66–74. https://doi.org/10.1016/j.jnucmat.2018.02.038.

[4]   X. Li, X. Li, S. Schönecker, R. Li, J. Zhao, L. Vitos, Understanding the mechanical properties of reduced activation steels, Mater. Des. 146 (2018) 260–272. https://doi.org/10.1016/j.matdes.2018.03.009.

[5]   R. Montanari, G. Filacchioni, B. Riccardi, M.. Tata, G. Costanza, Characterization of Eurofer-97 TIG-welded joints by FIMEC indentation tests, J. Nucl. Mater. 329–333 (2004) 1529–1533. https://doi.org/10.1016/J.JNUCMAT.2004.04.173.

[6]   S.J. Zinkle, J.L. Boutard, D.T. Hoelzer, A. Kimura, R. Lindau, G.R. Odette, M. Rieth, L. Tan, H. Tanigawa, Development of next generation tempered and ODS reduced activation ferritic/martensitic steels for fusion energy applications, Nucl. Fusion. 57 (2017).

[7]   M. Rieth, M. Schirra, A. Falkenstein, P. Graf, S. Heger, H. Kempe, R. Lindau, H. Zimmermann, EUROFER 97 Tensile, charpy, creep and structural tests, (2003) 68. http://inis.iaea.org/search/search.aspx?orig_q=RN:35032617.

[8]   P. Aubert, F. Tavassoli, M. Rieth, E. Diegele, Y. Poitevin, Low activation steels welding with PWHT and coating for ITER test blanket modules and DEMO, J. Nucl. Mater. 409 (2011) 156–162. https://doi.org/10.1016/J.JNUCMAT.2010.09.009.

[9]   S. Kirk, W. Suder, K. Keogh, T. Tremethick, A. Loving, Laser welding of fusion relevant steels for the European DEMO, Fusion Eng. Des. (2018). https://doi.org/10.1016/j.fusengdes.2018.03.039.

[10]   H. Tanigawa, T. Maruyama, Y. Noguchi, N. Takeda, S. Kakudate, Laser welding to expand the allowable gap in bore welding for ITER blanket hydraulic connection, Fusion Eng. Des. 98–99 (2015) 1634–1637. https://doi.org/10.1016/j.fusengdes.2015.06.155.

[11]   P. Aubert, F. Tavassoli, M. Rieth, E. Diegele, Y. Poitevin, Review of candidate welding processes of RAFM steels for ITER test blanket modules and DEMO, J. Nucl. Mater. 417 (2011) 43–50. https://doi.org/10.1016/J.JNUCMAT.2010.12.248.

[12]   D.J. Hughes, E. Koukovini-Platia, E.L. Heeley, Residual stress in a laser welded EUROFER blanket module assembly using non-destructive neutron diffraction techniques, Fusion Eng. Des. 89 (2014) 104–108. https://doi.org/10.1016/j.fusengdes.2013.12.041.

[13]   S. Kumar, A. Kundu, K.A. Venkata, A. Evans, C.E. Truman, J.A. Francis, K. Bhanumurthy, P.J. Bouchard, G.K. Dey, Residual stresses in laser welded ASTM A387 Grade 91 steel plates, Mater. Sci. Eng. A. 575 (2013) 160–168. https://doi.org/10.1016/j.msea.2013.03.046.

[14]   Y.Q. Wang, M.W. Spindler, C.E. Truman, D.J. Smith, Critical analysis of the prediction of stress relaxation from forward creep of Type 316H austenitic stainless steel, Mater. Des. 95 (2016) 656–668. https://doi.org/10.1016/j.matdes.2016.01.118.

[15]   J. Ahn, E. He, L. Chen, R.C. Wimpory, J.P. Dear, C.M. Davies, Prediction and measurement of residual stresses and distortions in fibre laser welded Ti-6Al-4V considering phase transformation, Mater. Des. 115 (2017) 441–457. https://doi.org/10.1016/j.matdes.2016.11.078.

[16]   D.G. Carr, M.I. Ripley, T.M. Holden, D.W. Brown, S.C. Vogel, Residual stress measurements

in a zircaloy-4 weld by neutron diffraction, Acta Mater. 52 (2004) 4083–4091. https://doi.org/10.1016/j.actamat.2004.05.021.

[17] W. Woo, G.B. An, E.J. Kingston, A.T. Dewald, D.J. Smith, M.R. Hill, Through-thickness distributions of residual stresses in two extreme heat-input thick welds: A neutron diffraction, contour method and deep hole drilling study, Acta Mater. 61 (2013) 3564–3574. https://doi.org/10.1016/j.actamat.2013.02.034.

[18] R.S. Ramadhan, A.K. Syed, A.S. Tremsin, W. Kockelmann, R. Dalgliesh, B. Chen, D. Parfitt, M.E. Fitzpatrick, Mapping residual strain induced by cold working and by laser shock peening using neutron transmission spectroscopy, Mater. Des. 143 (2018) 56–64. https://doi.org/10.1016/j.matdes.2018.01.054.

[19] A.S. Tremsin, J. V. Vallerga, J.B. McPhate, O.H.W. Siegmund, R. Raffanti, High resolution photon counting with MCP-timepix quad parallel readout operating at > 1 KHz frame rates, IEEE Trans. Nucl. Sci. 60 (2013) 578–585. https://doi.org/10.1109/TNS.2012.2223714.

[20] W. Kockelmann, T. Minniti, D.E. Pooley, G. Burca, R. Ramadhan, F.A. Akeroyd, G.D. Howells, C. Moreton-Smith, D.P. Keymer, J. Kelleher, S. Kabra, T.L. Lee, R. Ziesche, A. Reid, G. Vitucci, G. Gorini, D. Micieli, R.G. Agostino, V. Formoso, F. Aliotta, R. Ponterio, S. Trusso, G. Salvato, C. Vasi, F. Grazzi, K. Watanabe, J.W.L. Lee, A.S. Tremsin, J.B. McPhate, D. Nixon, N. Draper, W. Halcrow, J. Nightingale, Time-of-flight neutron imaging on IMAT@ISIS: A new user facility for materials science, J. Imaging. 4 (2018). https://doi.org/10.3390/jimaging4030047.

[21] A.S. Tremsin, S. Ganguly, S.M. Meco, G.R. Pardal, T. Shinohara, W.B. Feller, Investigation of dissimilar metal welds by energy-resolved neutron imaging, J. Appl. Crystallogr. 49 (2016) 1130–1140. https://doi.org/10.1107/S1600576716006725.

[22] Y. Poitevin, P. Aubert, E. Diegele, G. de Dinechin, J. Rey, M. Rieth, E. Rigal, A. von der Weth, J.-L. Boutard, F. Tavassoli, Development of welding technologies for the manufacturing of

European Tritium Breeder blanket modules, J. Nucl. Mater. 417 (2011) 36–42. https://doi.org/10.1016/J.JNUCMAT.2010.12.259.

[23] L.P. Jones, P. Aubert, V. Avilov, F. Coste, W. Daenner, T. Jokinen, K.R. Nightingale, M. Wykes, Towards advanced welding methods for the ITER vacuum vessel sectors, Fusion Eng. Des. 69 (2003) 215–220. https://doi.org/10.1016/S0920-3796(03)00341-7.

[24] R. Coppola, O. Asserin, P. Aubert, C. Braham, A. Monnier, M. Valli, E. Diegele, Characterization of residual stresses in Eurofer welded specimens: Measurements by neutron diffraction and comparison with weld modeling, J. Nucl. Mater. 417 (2011) 51–54. https://doi.org/10.1016/J.JNUCMAT.2010.12.051.

[25] F. Bachmann, R. Hielscher, H. Schaeben, Texture analysis with MTEX–free and open source software toolbox, in: Solid State Phenom., Trans Tech Publ, 2010: pp. 63–68.

[26] M.R. Daymond, M. Preuss, B. Clausen, Evidence of variation in slip mode in a polycrystalline nickel-base superalloy with change in temperature from neutron diffraction strain measurements, Acta Mater. 55 (2007) 3089–3102. https://doi.org/10.1016/j.actamat.2007.01.013.

[27] E. Oliver, J. Santisteban, J. James, M. Daymond, J. Dann, ENGIN-X user manual, ISIS. Rutherford-Applet. Lab. UK. (2004).

[28] R.B. V Larson A. C.; Dreele, General Structure Analysis System (GSAS); Los Alamos National Laboratory Report LAUR 86-748 , Los Alamos Natl. Lab. Los Alamos, NM,. (2004).

[29] M. Turski, S. Pratihar, L. Edwards, M.R. Daymond, M.E. Fitzpatrick, The effect of plastic anisotropy on the residual stress within a 316L stainless steel bead-on-plate specimen, Mater. Sci. Forum. 524–525 (2006) 677–684. https://doi.org/10.4028/www.scientific.net/msf.524-525.679.

[30] G.S. Pawley, Unit-cell refinement from powder diffraction scans, J. Appl. Crystallogr. 14 (1981) 357–361. https://doi.org/10.1107/s0021889881009618.

[31] T. Gnäupel-Herold, A.A. Creuziger, M. Iadicola, A model for calculating diffraction elastic constants, J. Appl. Cryst. 45 (2012) 197–206. https://doi.org/10.1107/S0021889812002221.

[32] T. Minniti, K. Watanabe, G. Burca, D.E. Pooley, W. Kockelmann, Characterization of the new neutron imaging and materials science facility IMAT, Nucl. Instruments Methods Phys. Res. Sect. A Accel. Spectrometers, Detect. Assoc. Equip. 888 (2018) 184–195. https://doi.org/https://doi.org/10.1016/j.nima.2018.01.037.

[33] C.A. Schneider, W.S. Rasband, K.W. Eliceiri, NIH Image to ImageJ: 25 years of image analysis, Nat. Methods. 9 (2012) 671–675. https://doi.org/10.1038/nmeth.2089.

[34] A.S. Tremsin, T.Y. Yau, W. Kockelmann, Non-destructive Examination of Loads in Regular and Self-locking Spiralock® Threads through Energy-resolved Neutron Imaging, Strain. 52 (2016) 548–558. https://doi.org/10.1111/str.12201.

[35] B. Roebuck, E.G. Bennett, A. Dickson, The measurement of uncertainty in grain size distribution. Interlaboratory exercise part 1-reference images, National Physical Lab., 1999.

[36] N.S. Rossini, M. Dassisti, K.Y. Benyounis, A.G. Olabi, Methods of measuring residual stresses in components, Mater. Des. 35 (2012) 572–588. https://doi.org/10.1016/j.matdes.2011.08.022.

[37] H.H. Lai, W. Wu, Practical examination of the welding residual stress in view of low-carbon steel welds, J. Mater. Res. Technol. (2020). https://doi.org/10.1016/j.jmrt.2020.01.004.

[38] W. Suder, S. Ganguly, S. Williams, A.M. Paradowska, P. Colegrove, Comparison of joining efficiency and residual stresses in laser and laser hybrid welding, Sci. Technol. Weld. Join. 16 (2011) 244–248. https://doi.org/10.1179/1362171810Y.0000000020.

[39] P. Staron, A. Schreyer, H. Clemens, S. Mayer, Neutrons and synchrotron radiation in engineering materials science : from fundamentals to applications, n.d.

[40] G. Song, J. Lin, J. Bilheux, Q. Xie, L. Santodonato, J. Molaison, H. Skorpenske, A. M. Dos Santos, C. Tulk, K. An, A. Stoica, M. Kirka, R. Dehoff, A. Tremsin, J. Bunn, L. Sochalski-Kolbus, H. Bilheux, Characterization of Crystallographic Structures Using Bragg-Edge Neutron

Imaging at the Spallation Neutron Source, J. Imaging. 3 (2017) 65. https://doi.org/10.3390/jimaging3040065.

[41]   P.J. Withers, M. Preuss, A. Steuwer, J.W.L. Pang, Methods for obtaining the strain-free lattice parameter when using diffraction to determine residual stress, J. Appl. Crystallogr. 40 (2007) 891–904. https://doi.org/10.1107/S0021889807030269.

[42]   Z. Wang, E. Denlinger, P. Michaleris, A.D. Stoica, D. Ma, A.M. Beese, Residual stress mapping in Inconel 625 fabricated through additive manufacturing: Method for neutron diffraction measurements to validate thermomechanical model predictions, Mater. Des. 113 (2017) 169–177. https://doi.org/10.1016/j.matdes.2016.10.003.

[43]   D.J. Hughes, M.N. James, D.G. Hattingh, P.J. Webster, The Use of Combs for Evaluation of Strain-free References for Residual Strain Measurements by Neutron and Synchrotron X-ray Diffraction, J. Neutron Res. 11 (2003) 289–293. https://doi.org/10.1080/10238160410001726765.

[44]   R. Dakhlaoui, V. Klosek, M.H. Mathon, B. Marini, Orientation stress field analysis in polycrystalline bcc steel using neutron diffraction, Acta Mater. 58 (2010) 499–509. https://doi.org/10.1016/j.actamat.2009.09.028.

[45]   Z.L. Hu, S.J. Yuan, X.S. Wang, G. Liu, H.J. Liu, Microstructure and mechanical properties of Al-Cu-Mg alloy tube fabricated by friction stir welding and tube spinning, Scr. Mater. 66 (2012) 427–430. https://doi.org/10.1016/j.scriptamat.2011.12.006.

[46]   Y.H. Lee, D. Kwon, Measurement of residual-stress effect by nanoindentation on elastically strained (1 0 0) W, Scr. Mater. 49 (2003) 459–465. https://doi.org/10.1016/S1359-6462(03)00290-2.

[47]   E.O. Hall, The Deformation and Ageing of Mild Steel: III Discussion of Results, Proc. Phys. Soc. Sect. B. 64 (1951) 747. https://doi.org/10.1088/0370-1301/64/9/303.

[48]   N.J. Petch, The cleavage strength of polycrystals, J. Iron Steel Inst. 174 (1953) 25–28.

[49]   H. Bhadeshia, R. Honeycombe, Steels: microstructure and properties, Butterworth-Heinemann,

2017.